Inverse Problems and Imaging
Volume 4, No. 2, 2010, 257–271
doi:10.3934/ipi.2010.4.257

THREE-DIMENSIONAL DENTAL X-RAY IMAGING BY COMBINATION OF PANORAMIC AND PROJECTION DATA

Nuutti Hyvönen

Aalto University
Institute of Mathematics, P.O.Box 1100
FI-00076 Aalto, Finland

Martti Kalke

PaloDex Group
P.O.Box 20
FI-04301 Tuusula, Finland

Matti Lassas

University of Helsinki
Department of Mathematics and Statistics
FI-00014 Helsinki, Finland

Henri Setälä

PaloDex Group
P.O.Box 20
FI-04301 Tuusula, Finland

Samuli Siltanen

University of Helsinki
Department of Mathematics and Statistics
FI-00014 Helsinki, Finland

Abstract. A novel three-dimensional dental X-ray imaging method is introduced, based on hybrid data collected with a dental panoramic device. Such a device uses geometric movement of the X-ray source and detector around the head of a patient to produce a panoramic image, where all teeth are in sharp focus and details at a distance from the dental arc are blurred. A digital panoramic device is reprogrammed to collect two-dimensional projection radiographs. Two complementary types of data are measured from a region of interest: projection data with a limited angle of view, and a panoramic image. Tikhonov regularization is applied to these data in order to produce three-dimensional reconstructions. The algorithm is tested with simulated data and real-world *in vitro* measurements from a dry mandible. Reconstructions from limited-angle projection data alone do provide the dentist with three-dimensional information useful for dental implant planning. Furthermore, adding panoramic data to the process improves the reconstruction precision in the direction of the dental arc. The presented imaging modality can be seen as a cost-effective alternative to a full-angle CT scanner.

2000 *Mathematics Subject Classification.* Primary: 92C55; Secondary: 65F22.

Key words and phrases. X-ray imaging, panoramic image, limited angle data, hybrid data, Tikhonov regularization, three-dimensional reconstruction.

1. **Introduction.** Dentists often need precise three-dimensional information about dental tissue for diagnosis and treatment. This is the case, for example, in detecting bone loss between teeth, in determining the spatial relationship between the roots of a wisdom tooth and close-by nerves, and in the main application considered in this work, dental implant planning. Dental implants are artificial teeth attached as follows: an oral surgeon drills a hole in the bone, a base is screwed into the hole, and the implant is attached to the base. The crucial task in dental implant planning is deciding the direction and depth of drilling: the hole must be deep enough to ensure firm attachment of the implant, but shallow enough for not harming any nerves.

How, then, can a dentist acquire such three-dimensional information? Every dental clinic has at least two different X-ray devices: chair-side intraoral X-ray device for taking two-dimensional projection images (or *radiographs*) of a few teeth at a time, and a panoramic device for taking a *panoramic image* showing all dental structures simultaneously. Panoramic images are produced using a special geometric movement of the X-ray source and detector around the head of a patient so that all teeth are in sharp focus and details at a distance from the dental arc are blurred, see [21, 30, 33] and Figure 1. However, intraoral radiographs and panoramic images are two-dimensional and do not always contain enough information due to overlapping of features.

Three-dimensional X-ray imaging tools for implant planning include (i) full-angle tomography with a *cone beam computed tomography* (CBCT) device designed for dental applications and (ii) limited-angle tomography using a panoramic device reprogrammed to collect projection data as shown by the blue lines in Figure 2. In this paper we study and extend option (ii), whose benefit over (i) is lower radiation dose and the possibility of using cost-effective standard equipment. On the negative side, there is a big mathematical difference between (i) and (ii). Namely, reconstruction from the comprehensive full-angle data provided by the CBCT device is only mildly ill-posed and results in high resolution [19], while reconstruction from the sparse limited-angle data provided by a panoramic device is a severely ill-posed inverse problem typically leading to reconstructions with elongation artifacts along projection directions; see [5, 26] and the references therein.

However, the goal of (ii) is not perfect recovery of the three-dimensional structure of the tissue, but instead a reconstruction good enough for implant planning. Indeed, limited-angle tomographic imaging using a panoramic device is realized commercially in the VT product of PaloDEx Group. The VT device has been shown to yield clinically useful three-dimensional information [3, 15].

The aim of this paper is to introduce and analyze an extension of (ii). In addition to the scanned projection images, it is possible to use the panoramic device to take a standard panoramic image of the patient. We call the collection of the projection images and the panoramic image the *hybrid data set*. The directions of the X-rays measured during the formation of the panoramic image are roughly perpendicular to the directions of the scanned projection radiographs, see Figure 2. Consequently, the hybrid data set is not so limited in view angle but rather represents a kind of sparse full-angle data. Thus, combining panoramic and projection data in the reconstruction process should yield improved three-dimensional information since more of the tissue boundaries are stably represented in the measurement [9, 22]. However, due to the narrow size of the detector area, the problem is an example of local tomography [9, 16, 24]. See [12, 13, 14, 15, 17, 20, 25, 27, 31] for related local tomographic reconstructions from sparse data. Also, since our added data is

not a projection image but a panoramic image whose structure is dependent on the specific movement of the X-ray source, the problem has a flavor of results on X-ray source moving on curves, see [10].

We compare three-dimensional reconstructions computed from the limited-angle projection data set to reconstructions obtained using the hybrid data set; the associated inverse problems are solved using Tikhonov regularization with a smoothness penalty [7, 29]. We consider two data sets collected from an *in silico* computer-based phantom and an *in vitro* dry mandible. The results suggest that a three-dimensional reconstruction from limited-angle projection data provides useful information for implant planning. Furthermore, incorporating panoramic data in the reconstruction process increases accuracy in the direction of the dental arc.

Tikhonov regularization is not the only possible solution methodology for the inverse problem considered here. For example, level set methods are another promising class of approaches, see [1, 6, 12, 18, 23, 28, 32].

Our results compensate for the shortcomings of hardware by computerized inversion methods: an affordable software upgrade to an existing digital panoramic device enables three-dimensional imaging even if a dental clinic is not able to invest in a CBCT device because of economical restrictions or lack of space. Reasonable cost of the proposed technology is especially important for improving healthcare in developing countries.

The use of data collected analogously to a panoramic dental imaging device may prove useful also outside the field of medical imaging. Potential application areas include wide-angle synthetic aperture radar imaging [4] and non-destructive testing [34].

This text is organized as follows. Section 2 introduces the used materials and inversion methods. In Section 3, we describe the obtained reconstructions. Finally, the significance of our findings is discussed in Section 4.

2. Materials and methods.

2.1. Structure of projection data.

The projection data sets used in this work consist of eleven radiographs taken with a limited angle of view of ± 21 degrees; see Figure 2 for an illustration of the projection geometry. In the case of real-world data, the two-dimensional projection radiographs are measured by moving the panoramic device so that the narrow *charge-coupled device* (CCD) sensor collects the transmitted X-rays.

We use the following linear measurement model for projection data:

$$m_1 = A_1 x, \tag{1}$$

where the vector x represents unknown voxel values of the attenuation in the tissue, vector m_1 contains all pixel values in the measured set of digital radiographs, and the matrix A_1 comes from the well-known (discrete) pencil beam model for X-ray attenuation.

Let us be a bit more precise. A single projection image is obtained by placing a (pointlike) X-ray source on one side of the object of interest $\Omega \subset \mathbb{R}^3$. The resulting radiation passes through the object and is detected on the other side. The attenuation coefficient $x : \Omega \to [0, \infty)$ gives the relative intensity loss of an X-ray travelling for a small distance $\mathrm{d}s$ at $s \in \Omega$, i.e.,

$$\frac{\mathrm{d}I}{I} = -x(s)\mathrm{d}s.$$

Thus, we have the relation

$$\int_{L_j} x(s)\,\mathrm{d}s = \log \tilde{I} - \log I_j, \tag{2}$$

where $L_j \in \mathbb{R}^d$ is the line segment between the source and the jth pixel of the detector, I_j is the measured intensity at that pixel, and $\tilde{I}$ is the intensity of an X-ray leaving the source. Notice that $\tilde{I}$ can be obtained via calibration. After post-processing, the data in a projection image can thus be interpreted as integrals of the attenuation coefficient over a certain set of lines. We gather these data in a real vector m_1, i.e.,

$$(m_1)_j := \int_{L_j} x(s)\,\mathrm{d}s. \tag{3}$$

By dividing Ω into voxels, the attenuation coefficient can be approximated by a piecewise constant function

$$x \approx \sum_k x_k \chi_k, \tag{4}$$

where x_k and χ_k are the constant attenuation value and the characteristic function of the kth voxel, respectively. According to (3), the measurement at the jth pixel of the detector can thus be approximated by

$$(m_1)_j \approx \sum_k (A_1)_{jk}\, x_k,$$

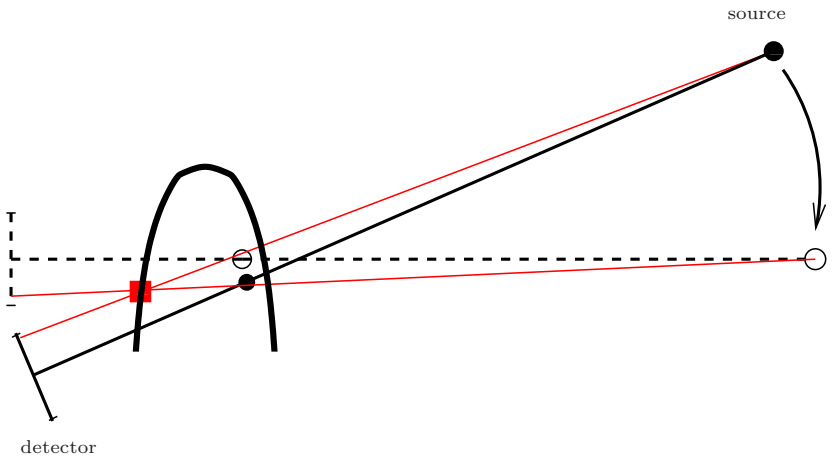

FIGURE 1. The generation of a panoramic image. As the device rotates, the CCD detector is operated so that the two X-rays (thin red lines) passing through a detail (red square) on the sharp layer (thick black curve) are recorded at the (approximately) same place on the panoramic image (although hitting different points on the detector itself). Intuitively, one can think that the 'film' is moved by the width of the detector between the recordings of the depicted X-rays.

where $(A_1)_{jk}$ denotes the length of the intersection of L_j with the kth voxel. This gives the needed discrete and linear measurement model for one position of the X-ray source; the whole linear system in (1) is obtained by gathering the measurement vectors and system matrices corresponding to different source positions on top of each other. For more information on the pencil beam model and its discretization, we refer to [13, 19, 26].

2.2. **Structure of panoramic data.** The formation of a panoramic image is illustrated in Figure 1. As the X-ray device rotates around the patient's head, the CCD detector is operated so that a sharp layer of image detail is recorded (that is, there is blurring of details that do not lie in the sharp layer). To be more precise, the idea is to record the X-rays travelling through a certain detail in the sharp layer at the same pixel of the panoramic image (see Figure 1). This works exactly only in the linear approximation of the measurement because the speed with which the 'film' (cf. Figure 1) needs to be moved depends on the particular point of the sharp layer. However, as the detector is relatively narrow (a few millimeters), it is a good approximation to interpret a pixel value in the (post-processed) panoramic image as a sum of integrals of the absorption over multiple lines that pass through a particular point of the sharp layer. As a consequence, the panoramic image can be considered as the restriction of a suitable (unfiltered) limited angle back-projection reconstruction to the sharp layer. This approach is used in Section 3.1, where our method is tested with simulated data.

We may also approximate the panoramic image formation process by discretizing the movement of the X-ray device: Assume that the device makes a divergent beam projection at some point in time, rotates to a new position and moves the 'film'

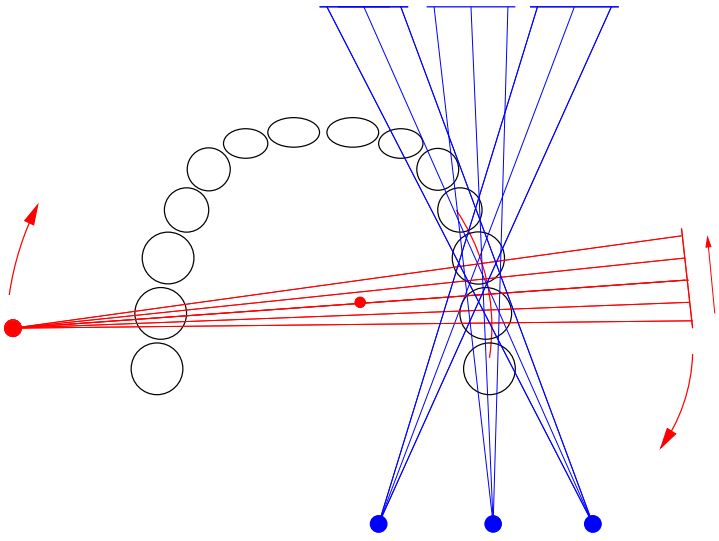

Figure 2. We collect two kinds of data. Projection data consists of a small number (less than a dozen) projections with directions roughly as shown by the blue (approximately vertical) lines. Panoramic data consists of the part of a panoramic image that shows the region of interest. The geometry of panoramic measurement is illustrated by the red (approximately horizontal) lines.

accordingly, makes another projection, and so on. This way the panoramic image can be considered as a sum of overlapping *virtual* X-ray projections, the formation of which can be handled by the discrete measurement model introduced in Section 2.1. This approximation is used in Section 3.2, where we consider real-world data obtained from a dry jaw specimen.

In all considered cases, we end up with the following linear measurement model for panoramic data:

$$m_2 = A_2 x.$$

As in Section 2.1, the vector x represents unknown voxel values of the attenuation in the tissue and vector m_2 contains all pixel values in the used part of the (post-processed) panoramic image. When real-world data is considered, the matrix A_2 accounts for modifying the discrete pencil beam model of Section 2.1 to cover the above described discrete approximation of panoramic imaging (see Section 3.2); in the case of the computer-based phantom, A_2 is obtained by considering suitable backprojection operators (see Section 3.1).

2.3. **Combining the two types of data.** The projection data (described in Section 2.1) and the panoramic data (described in Section 2.2) cannot be measured without detaching the patient from the imaging device between the two procedures. How can one calibrate the directions of the various X-rays so that the two data sets are related to the same coordinate system? The traditional clinical approach is to let the patient bite on a horseshoe-shaped plastic plate covered with a thick layer of special soft material. The material becomes solid in a short time, and the exact form of the patient's teeth is recorded. Both imaging sequences (projective and panoramic) are initiated by fixing the plastic plate (with tooth indentations) in the correct position within the panoramic X-ray device. The patient then bites the hardened "tooth relief" and holds still during the recording of the X-ray data. The directions of the X-rays can afterwards be calibrated from the projection images of fiducials, i.e., small steel balls attached to the plastic tooth relief.

2.4. **Test phantom and specimen.** The computer-based phantom used in our experiments is illustrated in the top left image of Figure 3: It is a transversal slice of a full-angle tomographic reconstruction of a mandible and consists of 150×150 pixels that represent the absorption level of the phantom. We examine the simulated phantom to be able to compare our reconstructions with a known ground truth. For simplicity, we restrict our attention to two-dimensional tomography: In the case of the simulated phantom, this is enough to demonstrate crucial features of our approach.

We also perform experiments with an *in vitro* dry mandible. This three-dimensional computation gives a more realistic understanding about the suggested hybrid data imaging modality.

2.5. **Regularized reconstruction method.** All our experiment settings lead to the measurement model

$$m = Ax + \varepsilon, \tag{5}$$

where m is a vector containing the measured pixel values and the vector x is composed of the unknown voxel values of the absorption. In the case of reconstruction from projection data only, we take $A = A_1$ and $m = m_1$ in (5). On the other hand,

when studying the combination of projection and panoramic data, we choose

$$A = \begin{bmatrix} A_1 \\ A_2 \end{bmatrix} \qquad \text{and} \qquad m = \begin{bmatrix} m_1 \\ m_2 \end{bmatrix}.$$

The vector ε represents random measurement error resulting from the discretization, the photon counting process and the electronic noise in the detector.

Let us briefly analyze the structure of the noise. Since the size of the detector is relatively small and the number of photons emitted by the source is very high, it is reasonable to assume that the number of photons leaving the source in the direction of any particular pixel is $\tilde{I}/\alpha$, where $\alpha > 0$ is the 'intensity' of a single photon (cf. Section 2.1). For simplicity, we set $\alpha = 1$. Assume that some of the photons hitting the jth pixel of the detector are detected and the others are not. Such measurement is corrupted by (at least) two types of noise: First, the detector is a photon counter, implying that the attenuated signal at each pixel is a stochastic counting process. Second, the photon count of each pixel is amplified, which causes electronic noise.

It is reasonable to assume that the amplification noise is multiplicative. Bearing in mind that the relation of the quantity m and the measured intensity involves a logarithm, see (2-3), a well-grounded model for the electronic noise in m is thus additive.

On the other hand, a feasible model for the counting process is to assume that the photon count of the jth pixel, n_j, is independent of n_l, $l \neq j$, and has the conditional probability density

$$\begin{aligned} p(n_j|x) &= p_{\,\text{Poisson}}(n_j, \lambda_j) \\ &= \frac{1}{n_j!}\lambda_j^{n_j} e^{-\lambda_j}, \end{aligned}$$

where x is the discrete attenuation from (4). The expectation value λ_j is given by

$$\lambda_j = \lambda_0 \tilde{I} \exp\Big(-\sum_k A_{jk} x_k \Big),$$

where $\lambda_0 > 0$ is the probability that a single photon hitting the detector is actually detected, and $\tilde{I}$ is the given initial intensity of an X-ray. Since in X-ray imaging a relatively large number of photons is usually detected at each pixel, the probability density of

$$M_j = \log \tilde{I} - \log I_j = \log \tilde{I} - \log n_j \tag{6}$$

can be approximated with a Gaussian probability distribution. Based on [2], the best Gaussian approximation is analyzed in detail in Appendix A of [26]. Here, we just recall the results obtained there. In what follows, we abuse the notation and denote by M_j the random variable that obeys this "best" Gaussian probability distribution.

The expectation of M_j is given by

$$\mu_j = \sum_k A_{jk} x_k - \log \lambda_0. \tag{7}$$

Since λ_0 can either be considered known, or alternatively it should be included also in the calibrated value of the initial intensity, i.e., $\tilde{I}$ in (6) should actually read $\lambda_0 \tilde{I}$, we may in the following neglect the term $\log \lambda_0$ in (7). The variance of M_j depends on the number of photons observed at the jth pixel. However, in practice the photon counts are typically of the same level of magnitude at all pixels, and we

may thus approximate the corresponding variances by a single positive constant η^2. By modeling the additive amplification noise caused by the electronics by Gaussian white noise with variance s^2, via slight abuse of notation we see that the (random) measurement vector $M = (M_j)$ is normally distributed:

$$M \sim N(\mu, D^2),$$

where the vector $\mu = (\mu_j)$ is composed of the expectation values (7) — without the term $\log \lambda_0$ included — and $D = \sigma^2 I$ is a diagonal matrix with $\sigma^2 = \eta^2 + s^2$.

Let us treat the discrete attenuation x as a realization of a random variable having the Gaussian distribution

$$x \sim N(0, \Sigma), \quad \Sigma = \delta L^{-1}, \tag{8}$$

where $\delta > 0$, and L is a discrete approximation of the Laplacian with Dirichlet boundary condition, obtained by using the standard five-point mask in dimension two and the seven-point mask in dimension three. Because the actual measurement m can be considered as a realization of the random variable M, finding the maximum a posterior estimate [8] for the attenuation values of the voxels is thus equivalent to minimizing the Tikhonov functional [29]

$$\|Ax - m\|_2^2 + \alpha \|Lx\|_2^2, \tag{9}$$

where $\alpha = \sigma^2/\delta^2$ and $\| \cdot \|_2$ denotes the Euclidean norm. In all our experiments, the reconstructions are computed by minimizing (9) with the conjugate gradient method [11]. Finally, it should be mentioned that no actual statistical techniques are used when choosing the regularization parameter $\alpha > 0$ for (9).

3. Results.

3.1. Reconstruction of simulated phantom.

The projection data corresponding to the computer-based phantom consists of 11 simulated parallel beam projections with a limited angle of view of ± 21 degrees with respect to the tangent of the sharp layer depicted by the dashed line in the top left image of Figure 3. Each simulated projection consists of 200 parallel line integrals. Notice that the formation of the parallel beam projections can be handled with the discrete pencil beam model of Section 2.1 under the assumption that the source is located infinitely far from the object of interest.

The panoramic data corresponds to a limited angle of view of ± 5 degrees with respect to the normal of the sharp layer; this kind of opening angle is encountered in standard panoramic X-ray devices. The data is simulated by taking 20 parallel beam projections (approximately along the normal of the sharp layer), computing the corresponding (unfiltered) limited angle backprojection image, and finally taking its restriction to the sharp layer. The panoramic radiograph is composed of 150 real numbers.

To avoid an obvious inverse crime, the reconstructions are computed on a sparser 140×140 grid. We simulate measurement noise by contaminating both of our data sets with white noise of zero mean and standard deviation of 0.02 times the maximum element of the data set in question.

In this section, $A_1 \in \mathbb{R}^{n_1 \times N}$ ($n_1 = 2200 = 11 \times 200$, $N = 19\,600 = 140 \times 140$) is the matrix that sends a vectorized 140×140 image onto the corresponding projection values (cf. Section 2.1). On the other hand, multiplication of a vectorized image by $A_2 \in \mathbb{R}^{n_2 \times N}$, $n_2 = 140$, produces the panoramic data. The matrix A_2 is constructed by taking the parallel beam projection matrix corresponding to the 20 directions

almost parallel to the normal of the sharp layer, multiplying it from the left by its transpose, which gives the corresponding limited angle backprojection operator, and finally deleting all rows that do not correspond to the 140 pixels in the sharp layer.

The first part of the data, $m_1 \in \mathbb{R}^{n_1}$, contains the noisy simulated projection values. The other part, $m_2 \in \mathbb{R}^{n_2}$, is obtained by taking the noisy vector containing the 150 simulated panoramic data values and interpolating it onto a sparser grid. The discrete approximation of the Laplacian appearing in (9) is constructed by using the standard five point mask.

In our computations, we used the value $\alpha = 0.01$ for the regularization parameter. The resulting reconstructions are illustrated in Figure 3, where the top left image shows the original phantom, the top right image is the reconstruction obtained from both projection and panoramic data, and the bottom left image illustrates the

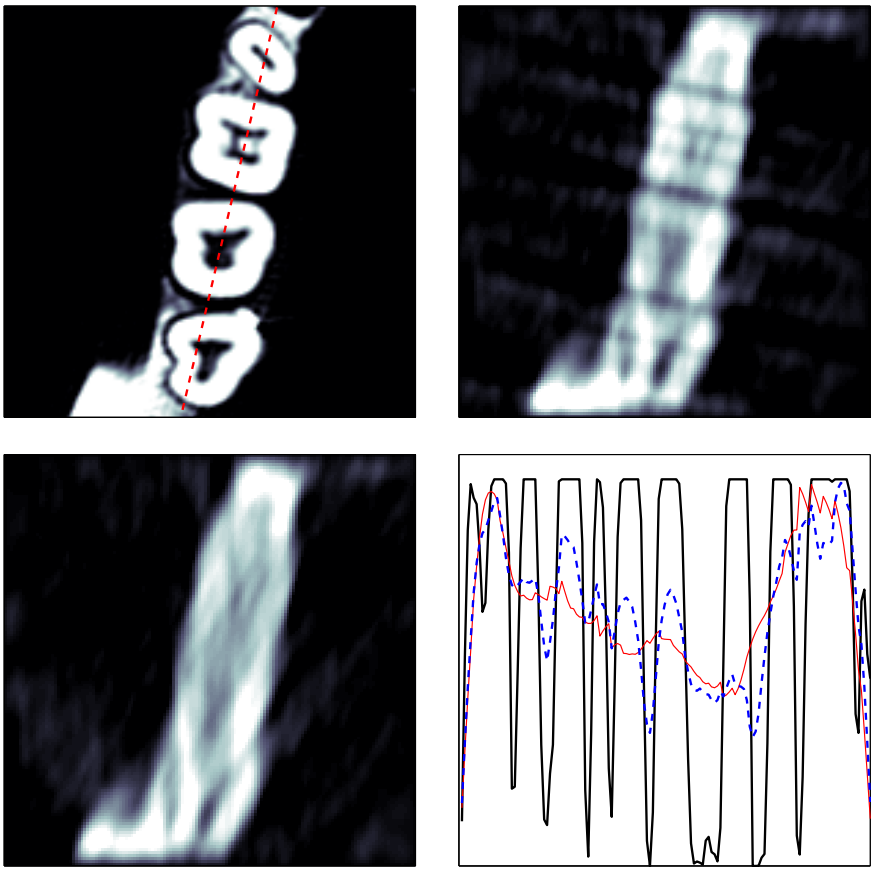

FIGURE 3. The reconstructions of the simulated phantom. Top left: the phantom. Top right: the reconstruction using both projection and panoramic data. Bottom left: the reconstruction using only projection data. Bottom right: the phantom (thick solid line), the top right reconstruction (dashed thick line), and the bottom left reconstruction (thin solid line) plotted along the sharp layer.

reconstruction computed using the same parameter values but only the projection data.

3.2. **Reconstruction from *in vitro* data.** For the dry jaw specimen, the projection data consists of 11 divergent beam projections with a limited angle of view of ± 21 degrees with respect to the left mandible. Two of the projections are shown in Figure 4.

The corresponding panoramic data set is illustrated in the right-hand image of Figure 5. It is constructed by taking a complete panoramic projection of the mandible (the left-hand image of Figure 5), and then restricting attention to the part that provides information on the *region of interest* (ROI). By using our knowledge of the alignment of the panoramic X-ray device during the measurement process, the data image is interpreted as a sum of 100 virtual overlapping and thin divergent beam projections taken at uniform time intervals; each pixel is typically treated as if it was obtained by summing ten pencil beam projections recorded at different positions of the measurement device. Because the angular speed of the panoramic device varies in time, the pixel values must be scaled in order to take into account the changes in the number of overlapping virtual projections. This explains the vertical stripes in the right-hand image of Figure 5.

When computing the reconstructions, the two data sets are aligned using the small metal pellets (fiducials) that are visible in Figures 4 and 5. Furthermore, the attenuation levels, i.e., the brightness, of the two data sets are matched by looking at certain well identifiable details in the corresponding X-ray images. Since this manual process cannot be considered totally reliable, the mismatch between the two data sets is bound to cause some artifacts in the reconstructions. If our method is to be used in commercial panoramic X-ray devices, this step of alignment and fine-tuning of the pixel values must be automated to obtain shorter processing times and more reliable reconstructions.

To arrive at a computational model, the surroundings of the left mandible are divided into $230 \times 150 \times 200$ cubic voxels with edge length 0.3mm. Here, the longest dimension corresponds approximately to the normal of the coronal plane, and the shortest one to the normal of the sagittal plane. Each of the eleven divergent beam projection images consists of 675×800 square pixels with edge length 0.096mm. The panoramic data set shown in the right-hand image of Figure 5 is composed of 700×450 pixels of this same size.

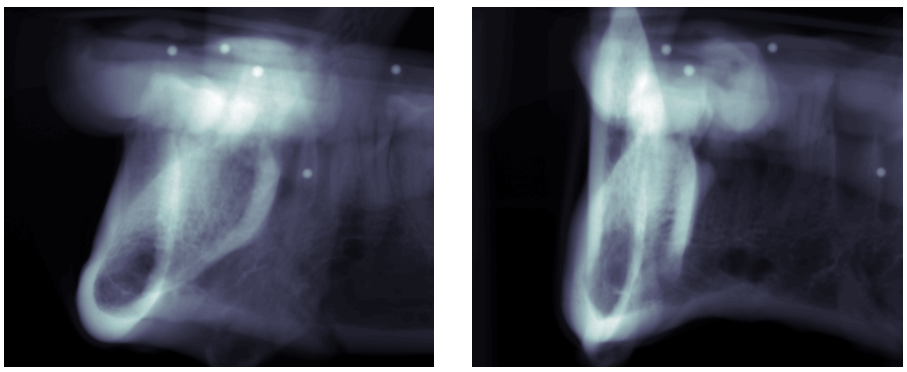

Figure 4. Two *in vitro* projection images of the mandible.

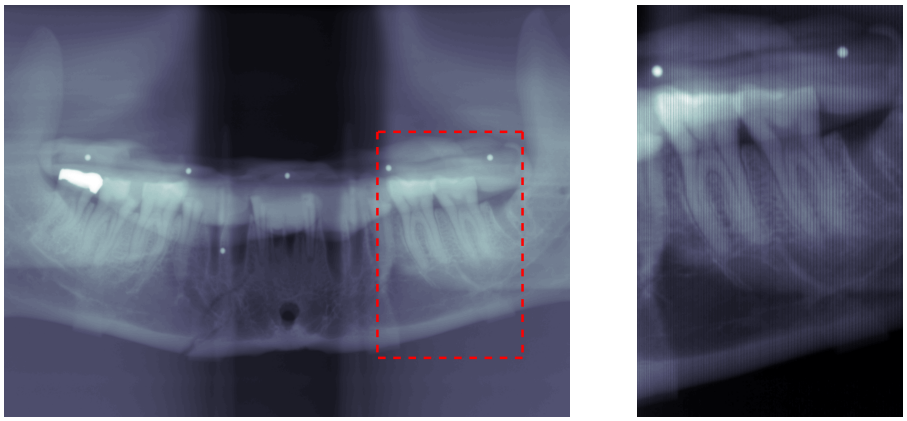

Figure 5. The panoramic images of the *in vitro* mandible. Left: The whole image with the region of interest highlighted. Right: The region of interest scaled so that it can be interpreted as a sum of multiple virtual projections.

In this section, $A_1 \in \mathbb{R}^{n_1 \times N}$ ($n_1 = 5\,940\,000 = 11 \times 675 \times 800$, $N = 6\,900\,000 = 230{\times}150{\times}200$) is the matrix that sends a vectorized 230×150×200 voxel volume onto the corresponding eleven projection images (see Section 2.1). The second matrix A_2 can be written as

$$A_2 = \sum_{j=1}^{100} A_2^{(j)},$$

where $A_2^{(j)} \in \mathbb{R}^{n_2 \times N}$, $n_2 = 315\,000 = 700{\times}450$, is the projection matrix corresponding to the jth (discrete) position of the X-ray device during the measurement of the panoramic data (see Sections 2.1 and 2.2). Because the device illuminates only about one tenth of the panoramic image shown in the right-hand image of Figure 5 at one time, most rows of each $A_2^{(j)}$ are empty; since each pixel of the panoramic image can be treated as a sum of about ten virtual pencil beam projections, any particular row of A_2 is nonempty in about ten $A_2^{(j)}$.

The first part of the data, $m_1 \in \mathbb{R}^{n_1}$, contains the eleven vectorized projection images, and the second part, $m_2 \in \mathbb{R}^{n_2}$, is the vectorized panoramic image. The discrete approximation of the Laplacian appearing in (9) is constructed by using the standard seven point mask. Take note that the measurement matrix A is sparse but so huge that it cannot be loaded into the memory in one part. Hence, the computations were conducted in a matrix free way, i.e., the needed matrix multiplications were computed one row at a time.

In our computations, we used the value $\alpha = 0.2$ for the regularization parameter; this value was chosen by trial and error with the help of expert knowledge about typical structure of a mandible. The need for a relatively large regularization parameter is explained by the modelling errors caused my the manual alignment and attenuation level matching of the two data sets (see Section 3.2). However, the quality of the reconstruction is not very sensitive to the parameter choice: All reconstructions for $\alpha \in [0.1, 0.5]$ are qualitatively similar.

The resulting three-dimensional reconstructions are presented in Figure 6, which illustrates a 128×128×128 subvolume around the ROI. The left column corresponds

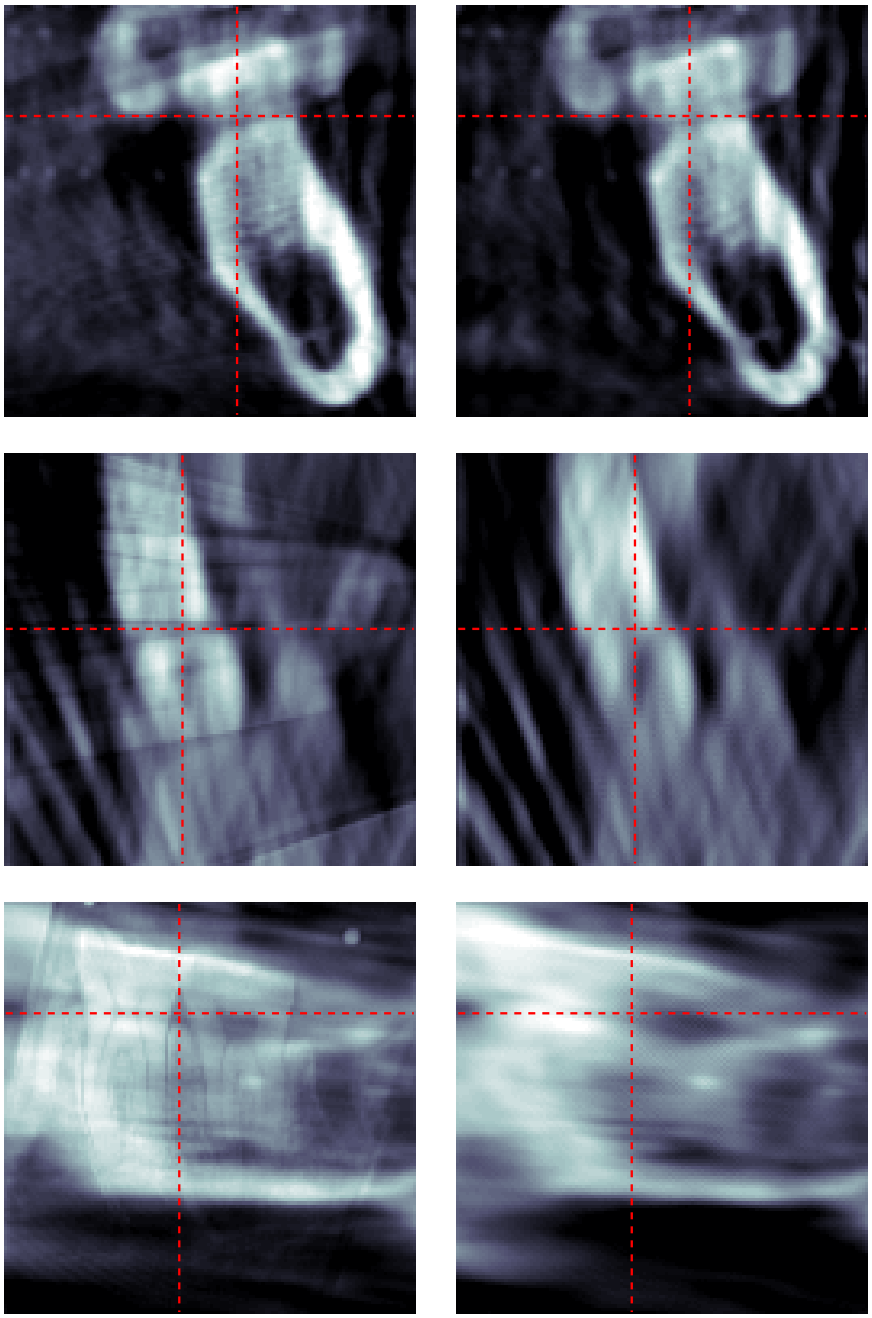

Figure 6. The reconstructions of the *in vitro* mandible. The left column illustrates the reconstruction from both data sets, and the right column the one from the projection data only. Top: a coronal slice. Middle: a transversal slice. Bottom: a sagittal slice. The dashed lines mark the locations of the other two slices.

to the reconstruction computed using both data sets, whereas the right column illustrates the reconstruction obtained from the projection data only. The first row of Figure 6 depicts a (approximately) coronal slice, the second row a transversal slice, and the third row a sagittal slice. In each image, the dashed lines mark the locations of the other two slices.

4. **Discussion.** In the experiment with the simulated phantom, the inclusion of panoramic data in the reconstruction process makes it possible to obtain information on the locations of the teeth along the mandible. Although the actual shapes of the teeth are not reconstructed properly, the gaps between the teeth are approximately at the right places. This observation is confirmed by the bottom right image of Figure 3, where the absorption distribution of the original phantom and of the two reconstructions are plotted along the sharp layer: The top right reconstruction oscillates in the same rhythm as the original phantom, whereas the bottom left reconstruction does not seem to resemble the original phantom in the direction of the mandible. Furthermore, the discrepancy in the Euclidean norm between the true phantom and the reconstruction in the top right image of Figure 3 is about 9% smaller than the one between the true phantom and the reconstruction in the bottom left image.

With regard to the reconstructions of the *in vitro* mandible, the incorporation of panoramic data into the reconstruction process provides once again information on the details along the mandible (Figure 6): In the coronal slice, the gap between the two molar teeth is visible only in the left-hand reconstruction. Similarly, the transversal slice contains information on the locations of the teeth only if the panoramic data is utilized. Finally, in the left-hand sagittal slice even small details of the molar teeth are visible, whereas the right-hand slice contains no such details. As in the case of the simulated phantom, the shapes of the molar teeth are not reconstructed exactly, but the locations of the teeth can be inferred from the left-hand slices of Figure 6. At the same time, it should be emphasized that the incorporation of the panoramic data does not seem to result in loss of any useful information. The fiducials used for aligning the measurement geometries cause artifacts in both reconstructions visualized in Figure 6. However, this phenomenon is about the same in both columns of Figure 6, and thus it does not affect the conclusion on the usefulness of hybrid data.

We conclude that crucial anatomical features can be seen in three-dimensional reconstructions from mere projection data. What is more, even the locations of such features along the dental arc become visible if panoramic data is included in the reconstruction process. This suggests that there is a strong possibility that a digital panoramic device can perform as the sole tool of an implantologist for three-dimensional X-ray imaging.

Acknowledgments. The research project was supported by PaloDEx Group and the Finnish Technology Agency (TEKES projects 2844/31/02 and 1107/401/00) and the Academy of Finland (Finnish Programme for Centres of Excellence in Research 2006–2011 and the project 115013). During part of the preparation of this work, SS worked as professor at the Department of Mathematics of Tampere University of Technology.

REFERENCES

[1] H. E. Abd El Munim, A. A. Farag and A. G. Farman, *A new variational approach for 3D shape registration*, 4th IEEE International Symposium on Biomedical Imaging: From Nano to Macro, (2007), 1324–1327.

[2] C. Bouman and K. Sauer, *A generalized Gaussian image model for edge-preserving MAP estimation*, IEEE Transactions on Image Processing, **2** (1993), 296–310.

[3] A. Cederlund, M. Kalke and U. Welander, *Volumetric tomography — a new tomographic technique for panoramic units*, Dentomaxillofac. Radiol., **38** (2009), 104–111.

[4] M. Cheney and B. Borden, *Problems in synthetic-aperture radar imaging*, Inverse Problems, **25** (2009), 123005.

[5] M. E. Davison, *The ill-conditioned nature of the limited-angle tomography problem*, SIAM J. Appl. Math., **43** (1983), 428–448.

[6] O. Dorn and D. Lesselier, *Level set methods for inverse scattering*, Inverse Problems, **22** (2006), R67–R131.

[7] H. Engl, M. Hanke and A. Neubauer, "Regularization of Inverse Problems," Mathematics and its Applications, 375, Kluwer Academic Publishers Group, Dordrecht, 1996.

[8] J. Kaipio and E. Somersalo, "Statistical and Computational Inverse Problems," Springer, 2004.

[9] A. I. Katsevich, *Local tomography for the limited-angle problem*, J. Math. Anal. Appl., **213** (1997), 160–182.

[10] A. Katsevich and M. Kapralov, *Filtered backprojection inversion of the cone beam transform for a general class of curves*, SIAM J. Appl. Math., **68** (2007), 334–353.

[11] C. T. Kelley, "Iterative Methods for Optimization," Frontiers in Applied Mathematics, 18, Society for Industrial and Applied Mathematics (SIAM), Philadelphia, PA, 1999.

[12] V. Kolehmainen, M. Lassas and S. Siltanen, *Limited data X-ray tomography using nonlinear evolution equations*, SIAM J. Sci. Comput., **30** (2008), 1413–1429.

[13] V. Kolehmainen, S. Siltanen, S. Järvenpää, J. P. Kaipio, P. Koistinen, M. Lassas, J. Pirttilä and E. Somersalo, *Statistical inversion for medical x-ray tomography with few radiographs: II. Application to dental radiology*, Phys. Med. Biol., **48** (2003), 1465–1490.

[14] V. Kolehmainen, A. Vanne, S. Siltanen, S. Järvenpää, J. P. Kaipio, M. Lassas and M. Kalke, *Parallelized Bayesian inversion for three-dimensional dental X-ray imaging*, IEEE Transactions on Medical Imaging, **25** (2006), 218–228.

[15] V. Kolehmainen, A. Vanne, S. Siltanen, S. Järvenpää, J. P. Kaipio, M. Lassas and M. Kalke, *Bayesian inversion method for 3D dental X-ray imaging*, Elektrotechnik & Informationstechnik, **124** (2007), 248–253.

[16] P. Kuchment, K. Lancaster and L. Mogilevskaya, *On local tomography*, Inverse Problems, **11** (1995), 571–589.

[17] C. Lehr and C.-E. Liedtke, *3D reconstruction of volume defects from few X-ray images*, Lec. Notes Comput. Sci., **1689** (1999), 275–284.

[18] S. Li, T. Fevens, A. Krzyżak and S. Li, *An automatic variational level set segmentation framework for computer aided dental X-rays analysis in clinical environments*, **30** (2006), 65–74.

[19] F. Natterer, "The Mathematics of Computerized Tomography," B. G. Teubner, Stuttgart; John Wiley & Sons, Ltd., Chichester, 1986.

[20] K. Niinimäki, S. Siltanen and V. Kolehmainen, *Bayesian multiresolution method for local tomography in dental X-ray imaging*, Phys. Med. Biol., **52** (2007), 6663–6678.

[21] Y. Paatero, *Pantomography and Orthopantomography*, Oral Surg. Oral Med. Oral Pathol., **14** (1961), 947–953.

[22] E. T. Quinto, *Singularities of the X-ray transform and limited data tomography in* $\mathbb{R}^2$ *and* $\mathbb{R}^3$, SIAM J. Math. Anal., **24** (1993), 1215–1225.

[23] R. Ramlau and W. Ring, *A Mumford-Shah level-set approach for the inversion and segmentation of X-ray tomography data*, J. Comput. Phys., **221** (2007), 539–557.

[24] A. G. Ramm and A. I. Katsevich, "The Radon Transform and Local Tomography," CRC Press, USA, 1996.

[25] M. Rantala, S. Vänskä, S. Järvenpää, M. Kalke, M. Lassas, J. Moberg and S. Siltanen, *Wavelet-based reconstruction for limited angle X-ray tomography,* IEEE Transactions on Medical Imaging, **25** (2006), 210–217.

[26] S. Siltanen, V. Kolehmainen, S. Järvenpää, J. P. Kaipio, J. Koistinen, M. Lassas, J. Pirttilä and E. Somersalo, *Statistical inversion for medical x-ray tomography with few radiographs: I. General theory*, Phys. Med. Biol., **48** (2003), 1437–1463.
[27] V. Singh, L. Mukherjee, P. M. Dinu, J. Xu and K. R. Hoffmann, *Limited view CT reconstruction and segmentation via constrained metric labeling*, Computer Vision and Image Understanding, **112** (2008), 67–80.
[28] X.-C. Tai and T. F. Chan, *A survey on multiple level set methods with applications for identifying piecewise constant functions*, Int. J. Numer. Anal. Model., **1** (2004), 25–47.
[29] A. N. Tikhonov, *Solution of incorrectly formulated problems and the regularization method*, Soviet Mathematics — Doklady, **4** (1963), 1035–1038.
[30] O. Tokuoka, *The principles of panoramic tomography*, Oral Radiology, **5** (1989), 31–38.
[31] S. Vänskä, M. Lassas and S. Siltanen, *Statistical X-ray tomography using empirical Besov priors*, International Journal of Tomography & Statistics, **11** (2009), 3–32.
[32] K. R. Varshney, N. Paragios, J.-F. Deux, A. Kulski, R. Raymond, P. Hernigou and A. Rahmouni, *Postarthroplasty examination using X-ray images*, IEEE Transactions on Medical Imaging, **28** (2009), 469–474.
[33] U. Welander, *Layer formation in narrow beam rotation radiography*, Acta Radiol. Diagn., **16** (1975), 529–540.
[34] J. Zhou, M. Maisl, H. Reiter and W. Arnold, *Computed laminography for materials testing*, Appl. Phys. Lett., **68** (1996), 3500–3502.

Received February 2009; revised December 2009.

E-mail address: nuutti.hyvonen@hut.fi
E-mail address: martti.kalke@palodexgroup.com
E-mail address: matti.lassas@helsinki.fi
E-mail address: henri.setala@palodexgroup.com
E-mail address: samuli.siltanen@helsinki.fi